Available online at www.sciencedirect.com

ScienceDirect

journal homepage: www.elsevier.com/locate/he

Nanorod-like NiFe metal-organic frameworks for oxygen evolution in alkaline seawater media

*Liyuan Xiao, Jingyi Han, Zhenlu Wang**, Jingqi Guan**

Institute of Physical Chemistry, College of Chemistry, Jilin University, 2519 Jiefang Road, Changchun, 130021, PR China

HIGHLIGHTS

- Ni_3Fe-BDC shows low η_{10} of 265 mV for the OER in 1 M KOH.
- Ni_3Fe-BDC shows η_{10} of only 280 mV for the OER in 1 M NaCl +1 M KOH.
- Ni_3Fe-BDC exhibits a low OER energy barrier of 13.7 kJ/mol.
- The in-situ formed rod-like Ni_3FeOOH serves as efficient active site for the OER.

GRAPHICAL ABSTRACT

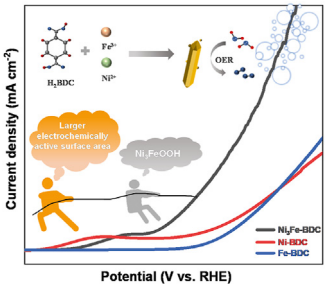

ARTICLE INFO

Article history:
Received 28 January 2023
Received in revised form
8 March 2023
Accepted 15 March 2023
Available online 2 April 2023

Keywords:
Nanorod
Metal organic framework
Ni_3FeOOH
Oxygen evolution reaction
Simulated seawater electrolysis

ABSTRACT

Searching for highly active and durable oxygen evolution reaction (OER) electrocatalysts is the key to break through the bottleneck of overall water splitting. Here, we prepare Ni_xFe-BDC (H_2BDC = terephthalic acid) nanorods with different Ni/Fe ratios by a facile solvothermal method for the OER. The optimal Ni_3Fe-BDC exhibits a low overpotential (η_{10}) of 265 mV and a Tafel slope of 90 mV·dec^{-1} in 1 M KOH. Moreover, it shows a low η_{10} of 280 mV and excellent stability in the mixture of 1 M NaCl and 1 M KOH, which has strong corrosion resistance to Cl^- anions. The role of Fe^{3+} not only increases the charge transfer rate of Ni_3Fe-BDC, but also affects the specific surface area of the catalyst with high electrochemical activity. Kinetic studies show that both Fe and Ni sites act as active centers, which catalyze synergistically to reduce the reaction kinetic energy barrier. Characterization results of the used Ni_3Fe-BDC reveal that the in situ formed rod-like Ni_3FeOOH is the active site for the OER.

* *Corresponding author.*
** *Corresponding author.*
E-mail addresses: wzl@jlu.edu.cn (Z. Wang), guanjq@jlu.edu.cn (J. Guan).
https://doi.org/10.1016/j.ijhydene.2023.03.233

Introduction

Water electrolysis can be used to produce sustainable, clean and high-calorie hydrogen for storing renewable energy, which can effectively alleviate the increasingly serious energy crisis. Water electrolysis includes hydrogen evolution reaction (HER) involving $2e^-$ transfer [1–3] and oxygen evolution reaction (OER) involving $4e^-$ transfer [4–6]. Thereinto, the rigid O–O double bond and $4e^-$ transfer process lead to slow OER kinetics [7,8], making OER the main dilemma of water splitting process. In recent years, people have been working to find efficient OER catalysts, such as transition metal oxides, sulfides, phosphides and selenides [9]. The catalytic performance of some catalysts even surpasses the benchmark electrocatalysts IrO_2 and RuO_2 [10,11]. Freshwater resources are scarce in the world, but seawater resources are abundant, accounting for about 96.5% of global water resources. Compared with electrolytic freshwater, seawater electrolysis can not only produce clean energy, but also desalinate seawater and solve the problem of freshwater demand in coastal arid areas [12,13]. Cl^- anions in seawater are the key to affect the electrolysis of seawater. In acidic medium, Cl^- anions can be easily converted to Cl_2 overflowing the water surface; while in alkaline media, Cl^- anions will be easily converted to ClO^- [14]. In addition, Cl^- anions will erode the electrode [15]. Thereby, OER catalysts with excellent catalytic activity, high conductivity and strong corrosion resistance are the targets that people are constantly looking for.

Since Ni/Fe-based composites have been reported to have excellent OER catalytic performance in 1987 [16], Ni/Fe-based catalysts have received great attention. Doping Fe into Ni-based catalysts can effectively modulate the local electronic environment of active sites [17], induce structural transformation, increase conductivity and improve the OER kinetics [18]. Zhang et al. prepared a p-p heterojunction (NiFe-PS) by doping nickel sulfide/nickel phosphide with Fe [19]. The built-in electric field at the interface promoted charge transfer, changed the electronic properties of NiFe-PS, improved conductivity, and thus enhanced catalytic activity. Chen et al. immobilized Fe-doped Ni oxyhydroxides in carbon nanotubes [20]. The coupling of Fe with NiOOH can adjust the mediator and reduce the reaction energy barrier, showing a low overpotential (η_{10}) of 264 mV. Zhao et al. prepared Fe-doped Ni_3S_2/MnS heterostructure catalyst on nickel foam (Fe–Ni_3S_2/MnS@NF), which showed a low η_{50} of 259 mV [21]. The Fe-doped heterostructure enhances the conductivity, optimizes the electronic configuration, and increases the adsorption capacity of *O and *OH. In recent years, Ni/Fe-based hydroxides have been proven to be effective for the OER. Hence, on this basis, people are constantly looking for various strategies to improve the catalytic activity of NiFe-based hydroxides by exposing more active sites through precisely designing dimensional topography, adjusting the electronic structure through manufacturing surface defects, and improving the electrical conductivity through combining with carbon materials. Li et al. synthesized Fe–$Ni(OH)_2$@NF on nickel foam (NF) [22]. The layered nanostructure enables the catalyst to exhibit more active sites, and the ultrathin nanosheets increase the electron transfer rate and enhance the OER catalytic activity. Sun et al. modified the layered Ni/Fe hydroxide by adding conductive carbon black (CB) to reduce the impedance of the material and improve the conductivity [23]. Metal-organic framework (MOF) has been widely used in the field of OER catalysis due to its high porosity, high specific surface area and unique adjustable structure [24]. In addition, its derivatives also overcome the shortcomings of poor conductivity and poor stability of the original MOF [25,26]. Different from single-metal MOFs, the synergistic effect between two different metals in bimetallic MOFs and the tunable metal node engineering are beneficial to improve the OER catalytic activity. Ni-based MOF itself has a unique spatial structure and high-density sites, and the incorporation of Fe increases the number of active sites. More importantly, Fe can also adjust the electron density of Ni 3d orbital, promoting the formation of OER intermediate *OOH [27]. Therefore, NiFe-MOF showed excellent OER catalytic activity [28]. Tan et al. prepared Ni9Fe1-BDC-0.15CB by doping Fe into metal organic framework (Ni) and adding CB to improve the charge transfer efficiency [29]. MOF itself has an ultra-high specific surface area, and the doping of Fe optimizes the electronic structure of Ni sites. In addition, metal species are highly dispersed in the MOF, which is conducive to exposing more active sites. Combining the above advantages, Ni9Fe1-BDC-0.15CB exhibited a low η_{10} of 290 mV. Jin et al. prepared bimetallic $[Ni_{2.87}Fe_{0.13}(HHTP)_2]_n$/CC on carbon cloth by in-situ growth method [30]. By combining MOF with carbon cloth, the conductivity is greatly improved and the electrochemical resistance is reduced. Using ultrathin amorphous Co/Ni/Fe MOFs as templates and metal sources, Li et al. in situ prepared three-dimensional layered microflowers (CoNiFe–OH) [31]. CoNiFe–OH has a rich mesoporous structure, 3D globular flower structure and high the specific surface area, which can reduce the ion diffusion distance, increase the material transfer rate and increase the number of active sites. The high stability and good durability of MOFs make them show greater potential in seawater electrolysis [32,33]. Zhang et al. used RuO_2 to modify NiFe-based MOF for seawater electrolysis [34]. In alkaline seawater electrolyte, the overpotential of RuO_2/NiFeOOH was 273.5 mV at 100 mA cm^{-2}, and the activity almost did not decline after 500 h continuous operation. The formation of heterostructure between RuO_2 and NiFeOOH is conducive to electron transfer, resulting in strong electron interaction and improved stability. Chen et al. modified MIL-88 (FeCoNi) by polypyrrole (PPy) and tannic acid (TA) to prepare hollow HMIL-88@PPy-TA [35]. TA was used as an etchant to transform MIL-88 into a hollow structure and capture the metal ions after etching. PPy can improve the stability and conductivity of the catalyst. In 1 M KOH + 0.5 M NaCl, HMIL-88@PPy-TA achieved a current density of 100 mA cm^{-2} at 244 mV. The electronic structure of the catalyst was optimized by PPy-TA, which can improve the anti-poisoning effect of chloride.

In this work, a series of bimetallic nanorod-like NiFe MOFs were prepared by a solvothermal method. When the Ni/Fe mole ratio is 3: 1, the obtained Ni_3Fe-BDC exhibited the best OER catalytic activity with an η_{10} of 265 mV. According to the kinetic study, the OER barrier of Ni_3Fe-BDC is as low as 13.7 kJ/mol, which is significantly lower than that of Ni-BDC (53.5 kJ/mol) and Fe-BDC (28.7 kJ/mol), indicating that Ni and Fe act as active

sites to reduce the OER kinetic barrier. In 1 M NaCl +1 M KOH, Ni_3Fe-BDC exhibited a low η_{10} of 280 mV, which showed strong corrosion resistance to Cl^- anions, and the current density did not change significantly after 25 h of continuous operation.

Results and discussion

Characterization of Ni_3Fe-BDC

The prepared route of nanorod-like Ni_xFe-BDC is shown in the Fig. 1a. In this experiment, Ni^{2+}, Fe^{3+} and terephthalic acid were coupled to form bimetallic Ni/Fe-MOF by solvothermal reaction (Fig. 1b). The morphology of Ni_3Fe-BDC was examined by SEM as shown in the Fig. 2a and b, which shows rod-like nano-sized crystals with a length of about 2–2.8 μm. From the element mapping image (Fig. 2c, d), O, Ni and Fe are uniformly distributed. HRTEM images show that the typical lattice spacing of Ni_3Fe-BDC is 0.938 nm (Fig. 2e–g). Fig. 2h shows that Ni_3Fe-BDC has three broad peaks at 2θ of about 10°, 38° and 44°, which are due to Ni-BDC (PDF#035–1677), indicating the existence of Ni-BDC structure. The diffraction peaks at 2θ of about 15°, 21° and 29° are ascribed to Fe-BDC (PDF#033–1723), indicating the successful incorporation of Fe in the obtained MOF. At the same time, from Fig. S1, the more the content of Fe element is, the worse the crystallinity is. Ni_3Fe-BDC exhibits a typical type IV isotherm (Fig. 2i), indicating a typical mesoporous structure. Ni_3Fe-BDC shows a specific surface area of 124.5 $m^2\ g^{-1}$ and an average pore size of 6.7 nm. The mesoporous structure can facilitate mass transfer and exposure of large active specific surface area.

OER performance

The OER performance of the as-prepared Ni_xFe-BDC was first evaluated in 1 M KOH solution, The LSV curves were collected with 90% iR compensation at a scan rate of 1 mV s^{-1}. As shown in Fig. 3a, Ni_3Fe-BDC exhibits an η_{10} of 265 mV, which is lower than that of Ni-BDC (350 mV), Fe-BDC (368 mV), benchmark RuO_2 (340 mV), and most previously reported NiFe-based electrocatalysts (Table S1), for instance, $Fe_2Ni_7S_8$ (359 mV) [36], CoFeNi @ CNT (440 mV) [37], $Ni_{0.9}Fe_{0.1}Se_2$ (285 mV) [38], Ni/Fe–COF@CNT_{900} (320 mV) [39], $Fe_{0.5}Ni_{0.5}$Pc-CP (315 mV) [40], Ni9Fe1-BDC-0.15CB (290 mV) [29], Fe(Ni)OOH (300 mV) [41], $Ni_{66}Fe_{34}$-NC (467 mV) [42], and NiCd(A)Fe (290 mV) [43]. The significant decrease in the overpotential from Ni-BDC and Fe-BDC to NiFe-BDC strongly indicates that a coordination mechanism between Ni and Fe plays an extremely important role in

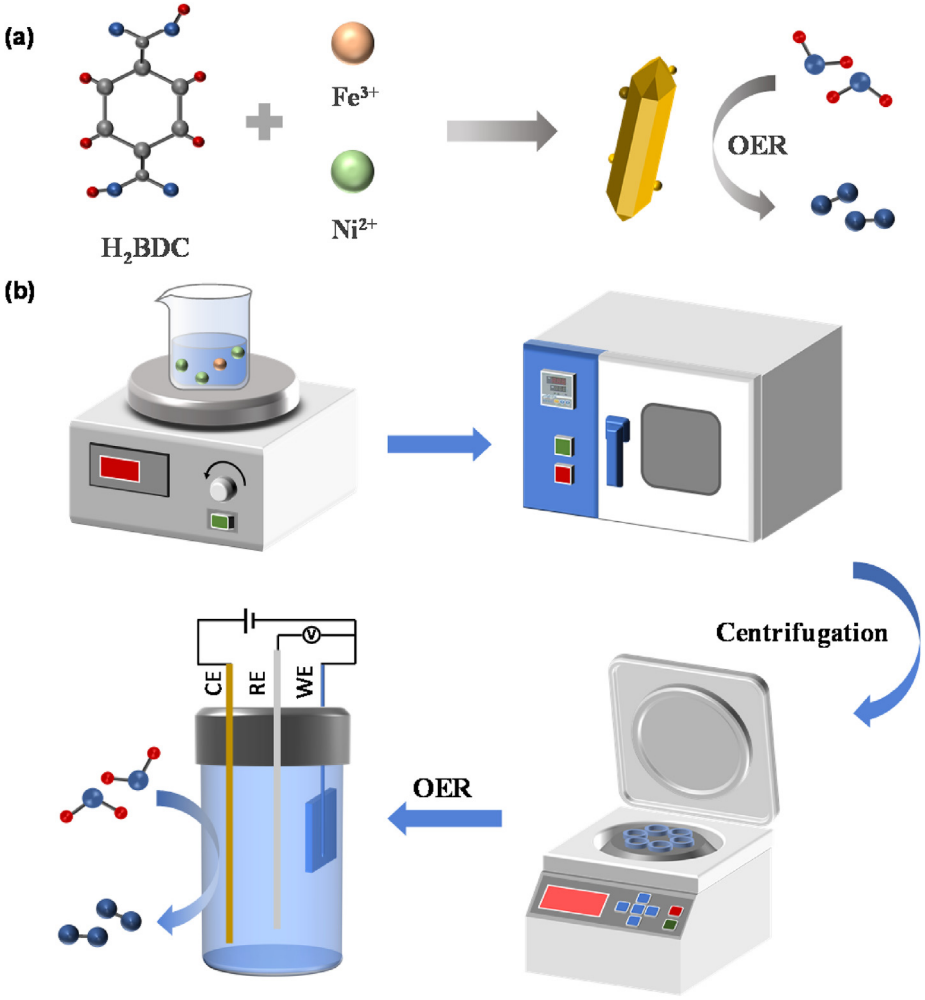

Fig. 1 – (a) Synthesis scheme and (b) synthetic route of Ni_xFe-BDC.

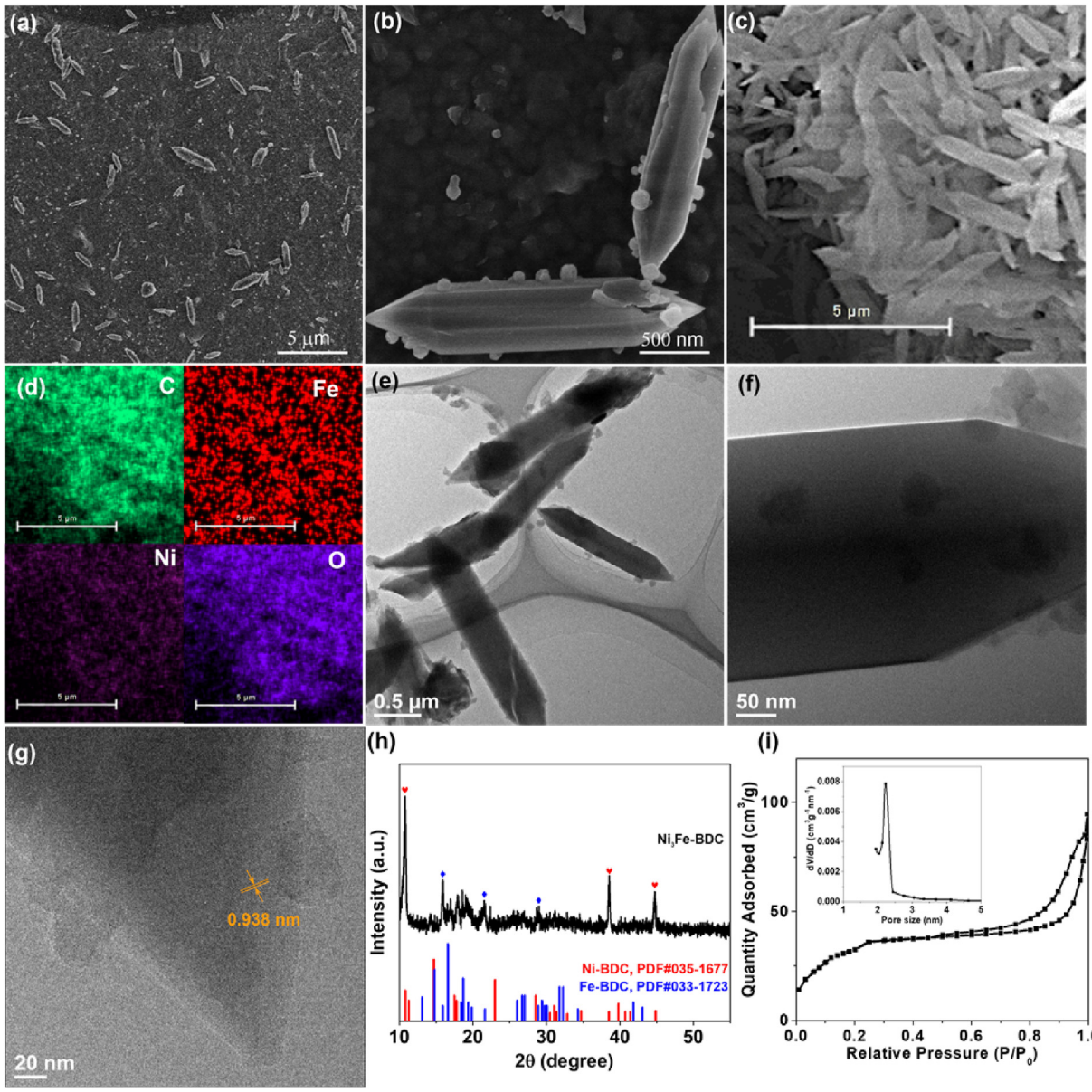

Fig. 2 – (a, b) SEM image of Ni_3Fe-BDC. (c) SEM image of Ni_3Fe-BDC used in the EDX. (d) EDX mapping. (e–g) HRTEM image of Ni_3Fe-BDC. (h) XRD patterns. (i) N_2 adsorption–desorption isotherms of Ni_3Fe-BDC (inset: pore size distribution).

OER electrocatalysis. The Tafel slope of Ni_3Fe-BDC is 90 $mV \cdot dec^{-1}$, which is lower than that of Ni-BDC (106 $mV \cdot dec^{-1}$) and Fe-BDC (154 $mV \cdot dec^{-1}$) (Fig. 3a), proving that Ni_3Fe-BDC has good kinetics. To investigate the role of Fe ions, different proportions of Ni_xFe-BDC (x = 1, 2, 3, 4, 5) were explored for the OER. From Fig. 3b, the OER polarization curve conforms to the volcanic trend, which is composed of the increase and decrease of the separated branches at x = 3. The η_{10} of Ni_1Fe-BDC, Ni_2Fe-BDC, Ni_4Fe-BDC and Ni_5Fe-BDC is 350 mV, 317 mV, 320 mV and 344 mV, respectively, and the corresponding Tafel slope is 105, 91, 92 and 135 mV dec^{-1} (Fig. 3c), indicating that the Ni/Fe ratio has a significant effect on the OER performance.

The kinetics of electron transfer process was studied by measuring the electrochemical impedance spectroscopy (EIS) of Ni_3Fe-BDC, Ni-BDC and Fe-BDC (Fig. 3d). According to the impedance arc in the semicircle of Nyquist impedance diagram, the charge transfer resistance (R_{ct}) of Ni_3Fe-BDC is 45 Ω cm^2, which is significantly lower than that of Fe-BDC (127 Ω cm^2) and Ni-BDC (790 Ω cm^2), confirming that the charge transfer efficiency increases obviously after Fe^{3+} doping into Ni-BDC. Thus, Ni_3Fe-BDC with fast charge transfer capability can promote OER kinetics. According to the Arrhenius formula $E_a = -2.3R\frac{\partial \log(i_k)}{\partial \frac{1}{T}}$, where i_k is the kinetic energy current at η = 300 mV, and R is the general gas constant. Ni_3Fe-BDC exhibits a low OER energy barrier of 13.7 kJ/mol (Fig. 3e and Fig. S2), which is much smaller than Ni-BDC (53.5 kJ/mol) and Fe (28.7 kJ/mol), indicating that the addition of Fe^{3+} modulates the valence state of Ni, enhances electron transfer,

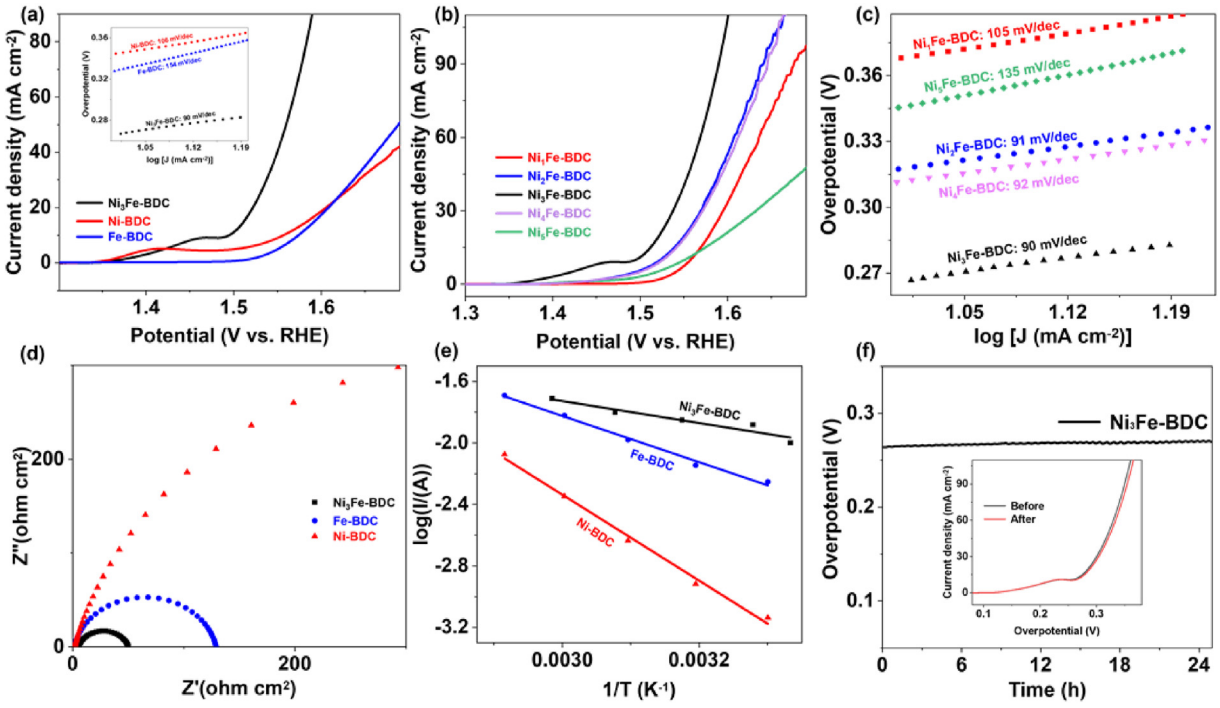

Fig. 3 – (a) LSV curves of Ni_3Fe-BDC, Ni-BDC and Fe-BDC (inset: Tafel slopes). (b) LSV curves and (c) Tafel slopes of Ni_xFe-BDC with different Ni/Fe ratios. (d) EIS plots. (e) Arrhenius plots. (f) Chronoamperometric responses.

and provides a strong driving force for the OER [44]. The ECSA of Ni_3Fe-BDC is determined to be 42 cm^2 (Fig. S3), which is higher than that of Ni-BDC (18 cm^2) (Fig. S4) and Fe-BDC (21 cm^2) (Fig. S5), indicating that Ni_3Fe-BDC has the largest ECSA. At the same time, the ECSA of Ni_1Fe-BDC, Ni_2Fe-BDC, Ni_4Fe-BDC and Ni_5Fe-BDC is 28, 35, 34 and 23 cm^2 (Figs. S6-S9), respectively, which are larger than those of Ni-BDC and Fe-BDC, indicating that bimetallic composite is more conducive to exposing larger ECSA than single metal. The synergistic effect between Ni and Fe sites increases the effective active

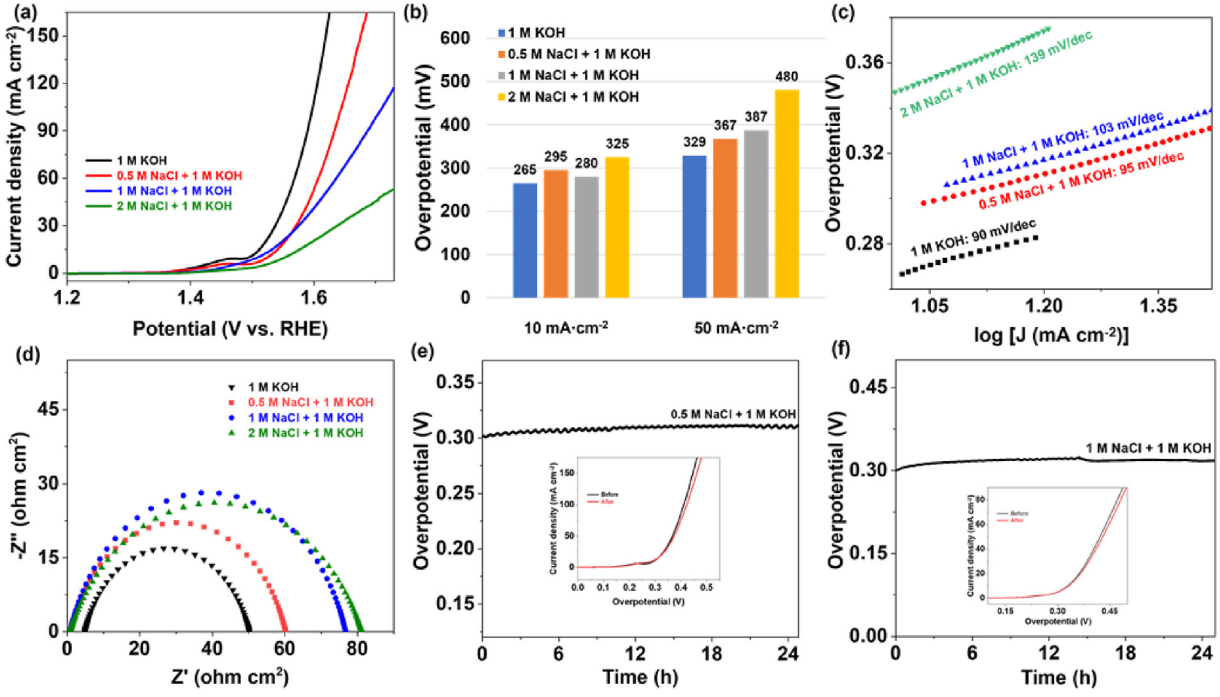

Fig. 4 – (a) LSV curves in different electrolytes. (b) The η_{10} and η_{50} of Ni_3Fe-BDC in different electrolytes. (c) Tafel slopes. (d) EIS plots. Chronoamperometric responses (e) in 0.5 M NaCl + 1 M KOH and (f) in 1 M NaCl + 1 M KOH.

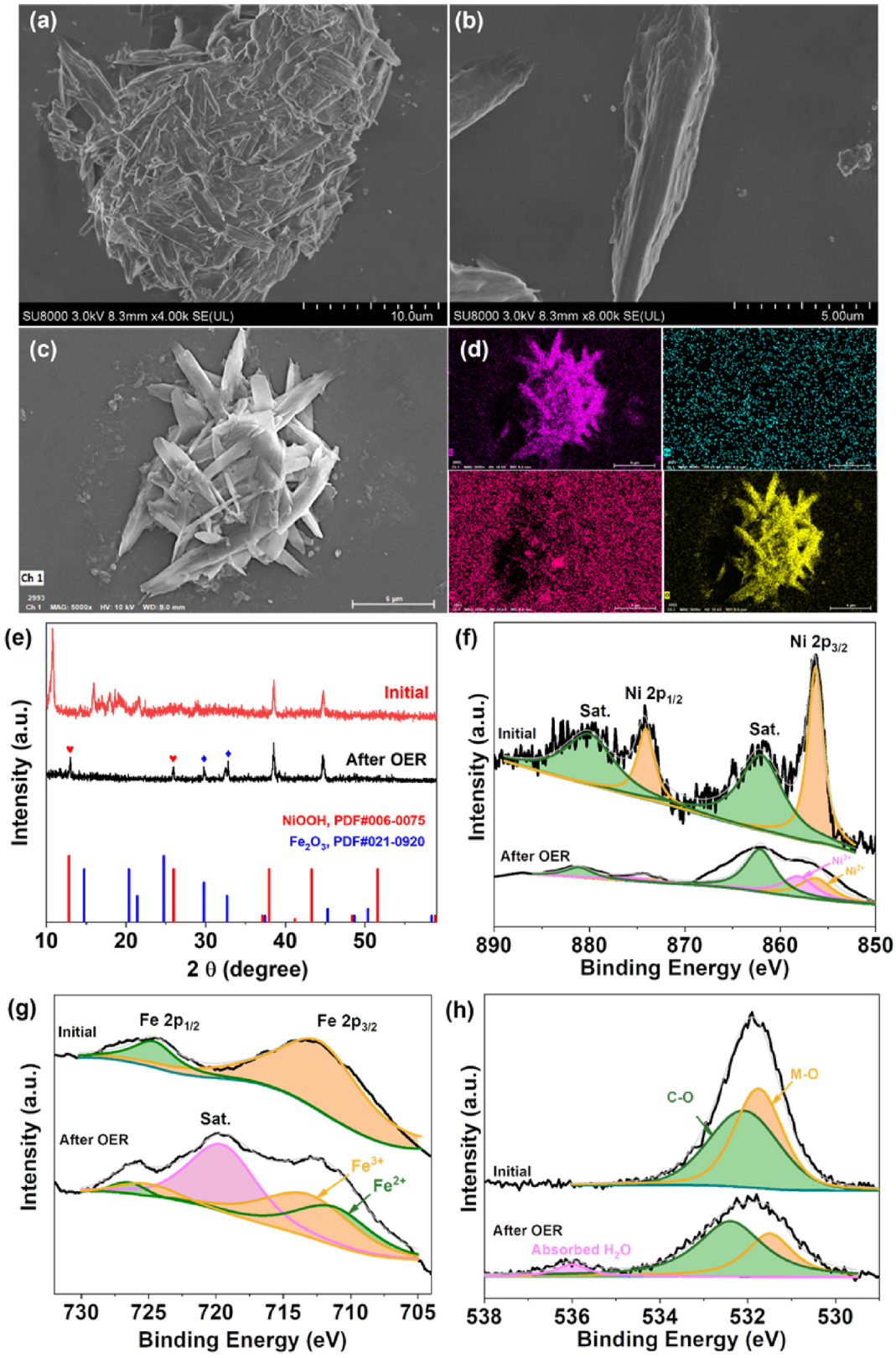

Fig. 5 – (a) and (b) SEM of the used Ni_3Fe-BDC. (c) SEM used in the EDX. (d) EDX of the used Ni_3Fe-BDC. (e) XRD pattern of the initial Ni_3Fe-BDC and the used Ni_3Fe-BDC. High-resolution (f) Ni 2p, (g) Fe 2p and (h) O 1s XPS spectra.

sites. When Fe^{3+} is added, the dilution effect will be produced, and the Ni^{3+} on the surface of the catalyst will be reduced [29]. Fe^{3+} can act as Lewis acid to attract electrons around Ni, which keeps Ni in a higher valence state [45]. Thereby, an appropriate Ni/Fe ratio can increase the exposed active specific surface area. Long-term stability is an important criterion for evaluating electrochemical catalysts. Fig. 3f shows the chronoamperometric curve of Ni_3Fe-BDC in 1 M KOH solution for long time electrolysis. After 25 h of measurement, Ni_3Fe-BDC can maintain excellent stability, which is due to that the strong synergy between Ni, Fe and O, and the mesoporous structure accelerates the separation of surface bubbles and promotes electron transport.

The OER activity of Ni_3Fe-BDC was then evaluated in alkaline simulated seawater (0.5 M NaCl + 1 M KOH, 1 M NaCl + 1 M KOH, 2 M NaCl + 1 M KOH) (Fig. 4a). The η_{10} on the Ni_3Fe-BDC in 0.5 M NaCl +1 M KOH, 1 M NaCl +1 M KOH, 2 M NaCl +1 M KOH is 295, 280 and 325 mV, respectively (Fig. 4b). At high current density (>30 mA cm^{-2}), Ni_3Fe-BDC has better OER performance with an η_{50} of 367 mV in 0.5 M NaCl + 1 M KOH solution, followed by 1 M NaCl + 1 M KOH solution with an η_{50} of 387 mV. In 0.5 M NaCl +1 M KOH and 1 M KOH +0.5 M NaCl electrolytes, the Tafel slopes of Ni_3Fe-BDC are 95 mV dec^{-1} and 103 mV dec^{-1}, respectively (Fig. 4c). Chlorine escape reaction (CER) is a two-electron reaction, which means that it is kinetically more favorable than a four-electron OER, but thermodynamically less favorable [46]. Thereby, CER can be thermodynamically suppressed below the overpotential of 480 mV [47]. To reach the current density of 50 mA cm^{-2}, Ni_3Fe-BDC needs overpotentials less than 480 mV in 0.5 M NaCl +1 M KOH and 1 M NaCl +1 M KOH. According to Fig. 4d, the R_{ct} of Ni_3Fe-BDC in 0.5 M NaCl +1 M KOH, 1 M NaCl +1 M KOH and 2 M NaCl +1 M KOH are 59, 76 and 81 Ω cm^2, respectively, which are higher than the charge transfer resistance in pure alkaline solution, indicating that the charge transfer ability decreases with the addition of NaCl. In high-salt electrolyte, stability and Cl-corrosion resistance are important factors to determine the quality of the catalyst. Fig. 4e and f shows that Ni_3Fe-BDC has excellent durability in both 0.5 M NaCl +1 M KOH and 1 M NaCl +1 M KOH electrolytes. The illustration shows that the compensated LSV curve measured after 25 h of continuous work has no significant change from the initial one. The above experiments show that the concentration of NaCl affects the OER performance of Ni_3Fe-BDC. With the increase of Cl^- ion concentration, the charge transfer ability in the OER decreases, which affects the reaction kinetics of Ni_3Fe-BDC. However, compared with those reported catalysts for simulated seawater electrolysis [48,49], the activity and stability of Ni_3Fe-BDC are still at a high level. Hence, Ni_3Fe-BDC has potential application prospect in low concentration seawater electrolysis.

After OER test, the morphology of Ni_3Fe-BDC was analyzed. Fig. 5a and b shows that the approximate morphology of the used Ni_3Fe-BDC still maintains a rod-like shape, but the surface becomes rough, and most of the edges and corners are missing due to structural transformation. According to EDX maps, Ni, Fe, C and O elements are still evenly distributed in the used Ni_3Fe-BDC (Fig. 5c and d). The XRD analysis of Ni_3Fe-BDC after OER test shows that some derivative peaks are missing in the XRD peaks after OER test, and some new characteristic peaks are presented. The newly added characteristic peaks at 2θ of about 13° and 25° are attributed to NiOOH (PDF#06–0075), and the derivative peaks at 2θ of about 29° and 32° are due to Fe_2O_3 (PDF#21–0920), indicating in-situ formed metal hydroxides (oxides) on the MOF surface. The measured XPS spectra show clear peaks of Ni 2p, Fe 2p, O 1s and C 1s (Fig. S10). The Ni 2p peak in the fresh Ni_3Fe-BDC can be split into Ni $2p_{3/2}$ (874.1 eV) and Ni $2p_{1/2}$ (856.3 eV) and two satellite peaks at 880.2 eV and 862.1 eV, characteristic of Ni^{2+}. After the OER test, the Ni $2p_{3/2}$ is divided into Ni^{3+} $2p_{3/2}$ (858.2 eV) and Ni^{2+} $2p_{3/2}$ (856.3 eV), and Ni $2p_{1/2}$ is divided into Ni^{3+} $2p_{1/2}$ (875.9 eV) and Ni^{2+} $2p_{1/2}$ (873.9 eV) (Fig. 5f). The surface relative content of Ni^{3+}/Ni^{2+} is estimated to be ca. 1.03/1, proving that NiOOH was produced during the OER. The Fe 2p peak in the fresh Ni_3Fe-BDC can be split into Fe $2p_{3/2}$ (724.9 eV) and Fe $2p_{1/2}$ (713.2 eV), characteristic of Fe^{3+}. After OER, a new satellite peak appears at 719.5 eV. The Fe $2p_{3/2}$ can be divided into Fe^{3+} $2p_{3/2}$ (713.1 eV) and Fe^{2+} $2p_{3/2}$ (711.2 eV) and Fe $2p_{1/2}$ can be divided into Fe^{3+} $2p_{1/2}$ (727.2 eV) and Fe^{2+} $2p_{1/2}$ (725.1 eV) (Fig. 5g). The surface relative content of Fe^{3+}/Fe^{2+} is estimated to be ca. 1/1.08. The O 1s in the fresh Ni_3Fe-BDC can be fitted into lattice Ni/Fe–O (531.7 eV) and C–O (532.1 eV) (Fig. 5h). After the OER test, the Ni/Fe–O and C–O peaks are significantly weakened and a peak at 536.0 eV is produced due to adsorbed water. The XPS results show that the addition of Fe modulates the electronic structure of the Ni site, promotes charge transfer, and produces interaction with Ni. NiOOH sites help to adsorb OER intermediates *OH and *OOH, Fe-doped NiOOH can adjust the d-band center of NiOOH [50–52], thereby modulating the adsorption capacity of OER intermediates. At the same time, Ni–O and Fe–O in the Ni_3FeOOH can improve the adsorption performance and charge transfer between intermediates and metal cations, and the generated oxygen vacancies can improve OER kinetics [53–55]. Hence, the rod-like Ni_3FeOOH formed in situ should be the reactive site towards efficient OER. The good stability is due to that the Ni–O and Fe–O sites play a major role in OER, and there are still metal-O vacancies even though metal (oxygen)hydroxides are formed, which can improve OER kinetics.

Conclusions

In summary, we have synthesized a nanorod-like Ni_3Fe-BDC metal-organic framework by a simple solvothermal reaction for efficient OER. In 1 M KOH and in 1 M NaCl +1 M KOH, Ni_3Fe-BDC shows low η_{10} of 265 mV and 280 mV, respectively. The excellent OER performance of Ni_3Fe-BDC can be attributed to the following: (1) Ni_3Fe-BDC shows a high specific surface area of 124.5 m^2 g^{-1} and an average pore size of 6.7 nm, which are conducive to exposing efficient active sites. (2) The addition of Fe can modulate the electronic structure of Ni sites and promote charge transfer. Moreover, Fe^{3+} itself can produce intrinsic active sites and improve OER catalytic activity. (3) The in-situ formed Ni_3FeOOH on the MOF surface serves as efficient active site for the OER. Kinetic studies show that Ni and Fe sites in the in situ formed Ni_3FeOOH synergistically reduce the OER kinetic barrier.

Declaration of competing interest

The authors declare that they have no known competing financial interests or personal relationships that could have appeared to influence the work reported in this paper.

Acknowledgments

This work was supported by the National Natural Science Foundation of China (No. 22075099), the Natural Science Foundation of Jilin Province (No. 20220101051JC), and the Education Department of Jilin Province (No. JJKH20220967KJ, No. JJKH20220968CY).

Appendix A. Supplementary data

Supplementary data to this article can be found online at https://doi.org/10.1016/j.ijhydene.2023.03.233.

REFERENCES

[1] Ding Y, Cao K-W, He J-W, Li F-M, Huang H, Chen P, et al. Nitrogen-doped graphene aerogel-supported ruthenium nanocrystals for pH-universal hydrogen evolution reaction. Chin J Catal 2022;43:1535–43. https://doi.org/10.1016/s1872-2067(21)63977.

[2] Xue Q, Bai X-Y, Zhao Y, Li Y-N, Wang T-J, Sun H-Y, et al. Au core-PtAu alloy shell nanowires for formic acid electrolysis. J Energy Chem 2022;65:94–102. https://doi.org/10.1016/j.jechem.2021.05.034.

[3] Ding Y, Miao B-Q, Jiang Y-C, Yao H-C, Li X-F, Chen Y. Polyethylenimine-modified nickel phosphide nanosheets: interfacial protons boost the hydrogen evolution reaction. J Mater Chem A 2019;7:13770–6. https://doi.org/10.1039/c9ta04283k.

[4] Han J, Niu X, Guan J. Unveiling the role of defects in iron oxyhydroxide for oxygen evolution. J Colloid Interface Sci 2023;635:167–75. https://doi.org/10.1016/j.jcis.2022.12.128.

[5] Tang T, Duan Z, Baimanov D, Bai X, Liu X, Wang L, et al. Synergy between isolated Fe and Co sites accelerates oxygen evolution. Nano Res 2022:2218–23. https://doi.org/10.1007/s12274-022-5001-3.

[6] Han JY, Guan JQ. Multicomponent transition metal oxides and (oxy)hydroxides for oxygen evolution. Nano Res 2022:1913–66. https://doi.org/10.1007/s12274-022-4874-7.

[7] Qiao C, Usman Z, Cao T, Rafai S, Wang Z, Zhu Y, et al. High-valence Ni and Fe sites on sulfated NiFe-LDH nanosheets to enhance O–O coupling for water oxidation. Chem Eng J 2021;426:130873. https://doi.org/10.1016/j.cej.2021.130873.

[8] Bai X, Wang L, Nan B, Tang T, Niu X, Guan J. Atomic manganese coordinated to nitrogen and sulfur for oxygen evolution. Nano Res 2022;15:6019–25. https://doi.org/10.1007/s12274-022-4293-7.

[9] Bai X, Duan Z, Nan B, Wang L, Tang T, Guan J. Unveiling the active sites of ultrathin Co-Fe layered double hydroxides for the oxygen evolution reaction. Chin J Catal 2022;43:2240–8. https://doi.org/10.1016/s1872-2067(21)64033-0.

[10] Bai X, Fan Y, Hou C, Tang T, Guan J. Partial crystallization of Co-Fe oxyhydroxides towards enhanced oxygen evolution activity. Int J Hydrogen Energy 2022;47:16711–8. https://doi.org/10.1016/j.ijhydene.2022.03.174.

[11] Tang T, Li S, Sun J, Wang Z, Guan J. Advances and challenges in two-dimensional materials for oxygen evolution. Nano Res 2022;15:8714–50. https://doi.org/10.1007/s12274-022-4575-0.

[12] Yu L, Wu L, McElhenny B, Song S, Luo D, Zhang F, et al. Ultrafast room-temperature synthesis of porous S-doped Ni/Fe (oxy)hydroxide electrodes for oxygen evolution catalysis in seawater splitting. Energy Environ Sci 2020;13:3439–46. https://doi.org/10.1039/d0ee00921k.

[13] Park YS, Lee J, Jang MJ, Yang J, Jeong J, Park J, et al. High-performance anion exchange membrane alkaline seawater electrolysis. J Mater Chem A 2021;9:9586–92. https://doi.org/10.1039/d0ta12336f.

[14] Chang J, Wang G, Yang Z, Li B, Wang Q, Kuliiev R, et al. Dual-doping and synergism toward high-performance seawater electrolysis. Adv Mater 2021;33:2101425. https://doi.org/10.1002/adma.202101425.

[15] Tan L, Yu J, Wang C, Wang H, Liu X, Gao H, et al. Partial sulfidation strategy to NiFe-LDH@FeNi2S4 heterostructure enable high-performance water/seawater oxidation. Adv Funct Mater 2022;32:2200951. https://doi.org/10.1002/adfm.202200951.

[16] Corrigan DA. The catalysis of the oxygen evolution reaction by iron impurities in thin film nickel oxide electrodes. J Electrochem Soc 1987;134:377–84.

[17] Ramesh SK, Son J, Ganesan V, Kim J. Carbon-incorporated Ni2P-Fe2P hollow nanorods as superior electrocatalysts for the oxygen evolution reaction. Nanoscale 2022:16262–9. https://doi.org/10.1039/d2nr02663e.

[18] Ding Y, Miao B-Q, Zhao Y, Li F-M, Jiang Y-C, Li S-N, et al. Direct growth of holey Fe3O4-coupled Ni(OH)(2) sheets on nickel foam for the oxygen evolution reaction. Chin J Catal 2021;42:271–8. https://doi.org/10.1016/s1872-2067(20)63639-7.

[19] Zhang J, Yu H, Yang J, Zhu X, Hu M, Yang J. Heterostructure engineering of the Fe-doped Ni phosphides/Ni sulfide p-p junction for high-efficiency oxygen evolution. J Alloys Compd 2022;924:166613. https://doi.org/10.1016/j.jallcom.2022.166613.

[20] Chen D, Sun Q, Han C, Guo Y, Huang Q, Goddard WA, et al. Enhanced oxygen evolution catalyzed by in situ formed Fe-doped Ni oxyhydroxides in carbon nanotubes. J Mater Chem A 2022;10:16007–15. https://doi.org/10.1039/d2ta04042e.

[21] Zhao M, Zhang S, Lin J, Hu W, Li CM. Synergic effect of Fe-doping and Ni3S2/MnS heterointerface to boost efficient oxygen evolution reaction. Electrochim Acta 2022;430:141088. https://doi.org/10.1016/j.electacta.2022.141088.

[22] Li L, Yuan C, Wang L, Xiang M, Zhang Q, Gao T, et al. In-system synthesize Fe nanodots-doped Ni hydroxide nanoflakes on Ni foam for efficient oxygen evolution catalysis. Electrochim Acta 2022;414:140232. https://doi.org/10.1016/j.electacta.2022.140232.

[23] Sun C, Wang T, Sun C, Li F. Layered double (Ni, Fe) hydroxide grown on nickel foam and modified by nickel carbonyl powder and carbon black as an efficient electrode for water splitting. Int J Hydrogen Energy 2022;47:19609–18. https://doi.org/10.1016/j.ijhydene.2021.11.160.

[24] Xiao LY, Wang ZL, Guan JQ. 2D MOFs and their derivatives for electrocatalytic applications: recent advances and new challenges. Coord Chem Rev 2022;472:214777. https://doi.org/10.1016/j.ccr.2022.214777.

[25] Gong W, Zhang H, Yang L, Yang Y, Wang J, Liang H. Core@shell MOFs derived Co2P/CoP@NPGC as a highly-active bifunctional electrocatalyst for ORR/OER. J Ind Eng Chem 2022;106:492–502. https://doi.org/10.1016/j.jiec.2021.11.032.

[26] Yang D, Chen Y, Su Z, Zhang X, Zhang W, Srinivas K. Organic carboxylate-based MOFs and derivatives for electrocatalytic

water oxidation. Coord Chem Rev 2021;428:213619. https://doi.org/10.1016/j.ccr.2020.213619.
[27] Li S, Gao Y, Li N, Ge L, Bu X, Feng P. Transition metal-based bimetallic MOFs and MOF-derived catalysts for electrochemical oxygen evolution reaction. Energy Environ Sci 2021;14:1897–927. https://doi.org/10.1039/d0ee03697h.
[28] Yaqoob L, Noor T, Iqbal N, Nasir H, Zaman N, Talha K. Electrochemical synergies of Fe-Ni bimetallic MOF CNTs catalyst for OER in water splitting. J Alloys Compd 2021;850:156583. https://doi.org/10.1016/j.jallcom.2020.156583.
[29] Tan J, He X, Yin F, Chen B, Liang X, Li G, et al. Fe doped metal organic framework (Ni)/carbon black nanosheet as highly active electrocatalyst for oxygen evolution reaction. Int J Hydrogen Energy 2020;45:21431–41. https://doi.org/10.1016/j.ijhydene.2020.05.230.
[30] Jin Y, Zhang T, Pan N, Wang S, Zhang B, Zhu X, et al. Surface functionalization of carbon cloth with conductive Ni/Fe-MOFs for highly efficient oxygen evolution. Surf Interfaces 2022;33:102294. https://doi.org/10.1016/j.surfin.2022.102294.
[31] Li X, Hou M, Qu X, Zhang Y, Li M. Electric-field assisted hydrolysis-oxidation of MOFs: hierarchical ternary (Oxy) hydroxide micro-flowers for efficient electrocatalytic oxygen evolution. Small 2022;18:2104863. https://doi.org/10.1002/smll.202104863.
[32] Wu D, Chen D, Zhu J, Mu S. Ultralow Ru incorporated amorphous cobalt-based oxides for high-current-density overall water splitting in alkaline and seawater media. Small 2021;17:2102777. https://doi.org/10.1002/smll.202102777.
[33] Huang Z-D, Feng C, Sun J-P, Xu B, Huang T-X, Wang X-K, et al. Ultrathin metal-organic framework nanosheets-derived yolk-shell Ni0.85Se@NC with rich Se-vacancies for enhanced water electrolysis. Ccs Chemistry 2021;3:2696–711. https://doi.org/10.31635/ccschem.020.202000537.
[34] Chang G, Zhou Y, Wang J, Zhang H, Yan P, Wu HB, et al. Dynamic reconstructed RuO2/NiFeOOH with coherent interface for efficient seawater oxidation. Small 2023. https://doi.org/10.1002/smll.202206768.
[35] Chen Y, Shen L, Wang C, Feng S, Zhang N, Zhang K, et al. Utilizing tannic acid and polypyrrole to induce reconstruction to optimize the activity of MOF-derived electrocatalyst for water oxidation in seawater. Chem Eng J 2022;430:132632. https://doi.org/10.1016/j.cej.2021.132632.
[36] Amin HMA, Attia M, Tetzlaff D. Apfel U.-P., tailoring the electrocatalytic activity of pentlandite FexNi9-XS8 nanoparticles via variation of the Fe : Ni ratio for enhanced water oxidation. Chemelectrochem 2021;8:3863–74. https://doi.org/10.1002/celc.202100713.
[37] Chen D, Li G, Chen X, Zhang Q, Sui J, Li C, et al. Developing nitrogen and Co/Fe/Ni multi-doped carbon nanotubes as high-performance bifunctional catalyst for rechargeable zinc-air battery. J Colloid Interface Sci 2021;593:204–13. https://doi.org/10.1016/j.jcis.2021.02.115.
[38] Li Y, Chen R, Yan D, Wang S. Regulation of morphology and electronic structure of NiSe(2)by Fe for high effective oxygen evolution reaction. Chem Asian J 2020;15:3845–52. https://doi.org/10.1002/asia.202000860.
[39] Xu Q, Qian J, Luo D, Liu G, Guo Y, Zeng G. Ni/Fe clusters and nanoparticles confined by covalent organic framework derived carbon as highly active catalysts toward oxygen reduction reaction and oxygen evolution reaction. Adv Sustain Syst 2020;4:2000115. https://doi.org/10.1002/adsu.202000115.
[40] Qi D, Chen X, Liu W, Liu C, Liu W, Wang K, et al. A Ni/Fe-based heterometallic phthalocyanine conjugated polymer for the oxygen evolution reaction. Inorg Chem Front 2020;7:642–6. https://doi.org/10.1039/c9qi01325c.
[41] Tang D, Mabayoje O, Lai Y, Liu Y, Mullins CB. In situ growth of Fe(Ni) OOH catalyst on stainless steel for water oxidation. Chemistryselect 2017;2:2230–4. https://doi.org/10.1002/slct.201700081.
[42] Ma M, Kumar A, Wang D, Wang Y, Jia Y, Zhang Y, et al. Boosting the bifunctional oxygen electrocatalytic performance of atomically dispersed Fe site via atomic Ni neighboring. Appl Catal, B 2020;274:119091. https://doi.org/10.1016/j.apcatb.2020.119091.
[43] Kim J-H, Youn DH, Kawashima K, Lin J, Lim H, Mullins CB. An active nanoporous Ni(Fe) OER electrocatalyst via selective dissolution of Cd in alkaline media. Appl Catal, B 2018;225:1–7. https://doi.org/10.1016/j.apcatb.2017.11.053.
[44] Wang M, Cao K, Tian Z, Sheng P. Increased charge and mass transfer derived-sheet-like Fe0.67Ni0.33OOH-Fe2O3@NF array for robust oxygen evolution reaction. Appl Surf Sci 2019;493:351–8. https://doi.org/10.1016/j.apsusc.2019.06.184.
[45] Li N, Bediako DK, Hadt RG, Hayes D, Kempa TJ, von Cube F, et al. Influence of iron doping on tetravalent nickel content in catalytic oxygen evolving films. Proc Natl Acad Sci U S A 2017;114:1486–91. https://doi.org/10.1073/pnas.1620787114.
[46] Zheng W, Lee LYS, Wong K-Y. Improving the performance stability of direct seawater electrolysis: from catalyst design to electrode engineering. Nanoscale 2021;13:15177–87. https://doi.org/10.1039/d1nr03294a.
[47] Zang W, Sun T, Yang T, Xi S, Waqar M, Kou Z, et al. Efficient hydrogen evolution of oxidized Ni-N-3 defective sites for alkaline freshwater and seawater electrolysis. Adv Mater 2021;33:2003846. https://doi.org/10.1002/adma.202003846.
[48] Yang L, Feng C, Guan C, Zhu L, Xia D. Construction of seaurchin-like structured Ag2Se-Ag2S-CoCH/NF electrocatalyst with high catalytic activity and corrosion resistance for seawater electrolysis. Appl Surf Sci 2023;607:154885. https://doi.org/10.1016/j.apsusc.2022.154885.
[49] Liu F, Hu R, Qiu H, Miao H, Wang Q, Yuan J. Constructing high-activity Cobalt-based Perovskite hybrid by a top-down phase evolution method for the direct seawater electrolysis anode. J Alloys Compd 2022;913:165342. https://doi.org/10.1016/j.jallcom.2022.165342.
[50] Li J, Song J, Huang B-Y, Liang G, Liang W, Huang G, et al. Enhancing the oxygen evolution reaction performance of NiFeOOH electrocatalyst for Zn-air battery by N-doping. J Catal 2020;389:375–81. https://doi.org/10.1016/j.jcat.2020.06.022.
[51] Friebel D, Louie MW, Bajdich M, Sanwald KE, Cai Y, Wise AM, et al. Identification of highly active Fe sites in (Ni,Fe)OOH for electrocatalytic water splitting. J Am Chem Soc 2015;137:1305–13. https://doi.org/10.1021/ja511559d.
[52] Mahala C, Sharma MD, Basu M. Fe-doped nickel hydroxide/nickel oxyhydroxide function as an efficient catalyst for the oxygen evolution reaction. Chemelectrochem 2019;6:3488–98. https://doi.org/10.1002/celc.201900857.
[53] Dong J, Wang Y, Jiang Q, Nan Z-A, Fan FR, Tian Z-Q. Charged droplet-driven fast formation of nickel-iron (oxy)hydroxides with rich oxygen defects for boosting overall water splitting. J Mater Chem A 2021;9:20058–67. https://doi.org/10.1039/d1ta05332a.
[54] Xing X-S, Ren X, Zeng X, Li A, Wang Y, Zhou Z, et al. Accelerating oxygen evolution reaction kinetics by reconstructing layered and defective Ni3FeOOH/FeOOH in a hematite photoanode. Solar RRL 2022:202201041. https://doi.org/10.1002/solr.202201041.
[55] Kathale BM, Xiao H, Yang S, Yin H, Yu T, Zhou X, et al. Fluoride mediated conversion of FeOOH into NiFeOOH for outstanding oxygen evolution reaction. Electrochim Acta 2022;406:139831. https://doi.org/10.1016/j.electacta.2022.139831.